

The Superconductivity of Sr_2RuO_4 Under c -Axis Uniaxial Stress

Fabian Jerzembeck,¹ Henrik S. Røising,² Alexander Steppke,¹ Helge Rosner,¹ Dmitry A. Sokolov,¹ Naoki Kikugawa,³ Thomas Scaffidi,⁴ Steven H. Simon,⁵ Andrew P. Mackenzie,^{1,6} and Clifford W. Hicks^{7,1}

¹*Max Planck Institute for Chemical Physics of Solids, Nöthnitzer Str 40, 01187 Dresden, Germany*

²*Nordita, KTH Royal Institute of Technology and Stockholm University,
Hannes Alfvéns väg 12, SE-106 91 Stockholm, Sweden*

³*National Institute for Materials Science, Tsukuba 305-0003, Japan*

⁴*Department of Physics, University of Toronto, Toronto, Ontario, M5S 1A7, Canada*

⁵*Rudolf Peierls Center for Theoretical Physics, Oxford OX1 3PU, United Kingdom*

⁶*Scottish Universities Physics Alliance, School of Physics and Astronomy,
University of St. Andrews, St. Andrews KY16 9SS, United Kingdom*

⁷*School of Physics and Astronomy, University of Birmingham, Birmingham B15 2TT, United Kingdom*

(Dated: January 19, 2022)

Applying in-plane uniaxial pressure to strongly correlated low-dimensional systems has been shown to tune the electronic structure dramatically. For example, the unconventional superconductor Sr_2RuO_4 can be tuned through a single Van Hove singularity which results in a strong enhancement of both T_c and H_{c2} . Out-of-plane (c axis) uniaxial pressure is expected to tune the quasi-two-dimensional structure even more strongly, causing it to approach two Van Hove singularities simultaneously. Here we achieve a record value of 3.2 GPa compression along the c axis of Sr_2RuO_4 . Although the rise in H_{c2} shows that we are indeed approaching the van Hove points, T_c is suppressed, a result that contradicts expectations based on simple two-dimensional models. As a first attempt to take the third dimension into account, we present three-dimensional calculations in the weak interaction limit, and discuss the extent to which they are consistent with observation. Our experimental results highlight the importance of out-of-plane effects in low-dimensional systems in general and provide new constraints on theories of the pairing interaction in Sr_2RuO_4 .

INTRODUCTION

Sr_2RuO_4 is a famous exemplar of unconventional superconductivity, due to the quality of the available samples and the precision of knowledge about its normal state, and because the origin of its superconductivity remains unexplained in spite of strenuous effort [1–4]. No proposed order parameter is able straightforwardly to account for all the existing experimental observations. The greatest conundrum is posed by evidence that the order parameter combines even parity [5–8] with time reversal symmetry breaking [9–11]. This combination of properties implies, if there is no fine tuning, that the superconducting order parameter is $d_{xz} \pm id_{yz}$ [12]. Under conventional understanding, this is not expected because the horizontal line node at $k_z = 0$ implies interlayer pairing, while the electronic structure of Sr_2RuO_4 is highly two-dimensional [13, 14].

This puzzle has led to substantial theoretical activity. Two recent proposals are $s \pm id$ [15, 16] and $d \pm ig$ [17, 18] order parameters, which require tuning to obtain $T_{\text{TRSB}} \approx T_c$ (where T_{TRSB} is the time reversal symmetry breaking temperature), but avoid horizontal line nodes. A mixed-parity state [19] and superconductivity that breaks time reversal symmetry only in the vicinity of extended defects [20] have been proposed to account for the absence of a resolvable heat capacity anomaly at T_{TRSB} [21]. Interorbital pairing through Hund’s coupling is also under discussion [22–25]; this mechanism could yield $d_{xz} \pm id_{yz}$ order without inter-

layer pairing. Thermal conductivity and quasiparticle interference data, on the other hand, have been interpreted as evidence for a single-component, d_{xy} or $d_{x^2-y^2}$ gap [26, 27].

Uniaxial stress has become an important probe of the superconductivity of Sr_2RuO_4 . When stress is applied along the [100] direction, the largest Fermi surface sheet (the γ sheet— see Fig. 1) distorts anisotropically, and undergoes a Lifshitz transition from an electron-like to an open geometry at -0.75 GPa (where negative values denote compression) [28]. T_c increases from 1.5 K in unstressed Sr_2RuO_4 to 3.5 K, while the c -axis upper critical field H_{c2} increases by a factor of twenty [29]. It is difficult to obtain such a strong H_{c2} enhancement without a gap that is large at the point in k -space where the transition occurs and the Fermi velocity falls nearly to zero— this would be the Y point for compression along [100], for example. In a two-dimensional picture, this point is parity-invariant, so the gap of odd-parity order parameters must vanish there, and the critical enhancement was therefore an early indication that the order parameter had to be even parity [29].

Naively, then, T_c and H_{c2} might be expected to rise even further under compression along the c axis. This raises the energy of the d_{xz} and d_{yz} bands relative to the d_{xy} band, and the resulting transfer of carriers expands the γ sheet, pushing it towards a Lifshitz transition from an electron-like to a hole-like geometry [30]. This transition occurs at both the X and Y points— see Fig. 1(c-d)— so the increase in the Fermi-level density of

states (DOS) as it is approached is expected to be larger than for the electron-to-open Lifshitz transition induced by in-plane stress. This electron-to-hole transition has been approached, and crossed, in thin films through epitaxial strain, and in bulk crystals by substitution of La for Sr [31–33], but in both cases the superconductivity was suppressed by disorder.

In this paper, we report uniaxial stress experiments up to 3.2 GPa along the c axis of Sr_2RuO_4 . This is a record value for bulk Sr_2RuO_4 and was achieved by using a focused ion beam as a novel sample preparation technique. Measurements of H_{c2} confirm the qualitative expectation that the γ Fermi surface sheet is driven towards both van Hove points. However, T_c decreases instead of increasing: Approaching the Lifshitz transition at either the X or Y point dramatically enhances T_c , while approaching both suppresses T_c . This is a major surprise, and is completely inconsistent with the simple two-dimensional models for the superconductivity that have dominated the field until now. In a first attempt to address this issue, and include effects related to the third dimension, we present calculations in the limit of weak coupling. Although these show that c -axis compression reduces the transition temperatures of certain order parameters, no order parameter could be identified for which the effects of out-of-plane and in-plane pressure were both captured. This highlights the need for other classes of theory to take c -axis pressure explicitly into account in the ongoing quest to identify the form of the pairing interaction and order parameter of Sr_2RuO_4 .

RESULTS

Electronic structure calculations

We start with density functional theory calculations of Sr_2RuO_4 under c -axis compression as a guide to the likely effects of strain on the electronic structure. Unstrained lattice parameters were taken from the $T = 15$ K data of Ref. [34]. Longitudinal strain ε_{zz} is taken as the independent variable, and ε_{xx} and ε_{yy} are set following the low-temperature Poisson's ratio from Ref. [35], which is 0.223 for stress along the c axis. Calculations were performed as described in Ref. [29]. We note in particular that spin-orbit coupling was treated nonperturbatively by solving the four-component Kohn-Sham-Dirac equation [36], the calculation was done in the local density approximation, and, due to proximity of a Van Hove singularity to the Fermi level, calculations were carried out on a fine-scale mesh in k space. The apical oxygen position was relaxed.

Results are shown in Fig. 1. The electron-to-hole Lifshitz transition is predicted to occur at $\varepsilon_{zz} = -0.025$ (where negative values denote compression). Low-temperature ultrasound data give a c -axis Young's modulus of 219 GPa [35], so this corresponds to stress $\sigma_{zz} \approx$

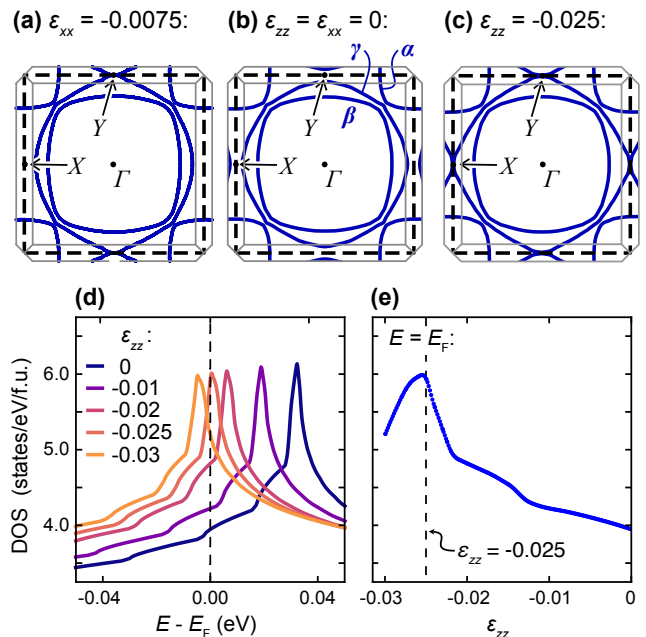


FIG. 1. (a–c) $k_z = 0$ slices through the calculated Fermi surfaces of Sr_2RuO_4 at the indicated strains. The heavy dashed lines indicate the zone of the RuO_2 sheet, and the thin gray lines the 3D zone of Sr_2RuO_4 . X and Y label high-symmetry points of the RuO_2 zone. To simplify discussion, we refer throughout this paper to the X and Y points defined in the 2D zone. (a) The electron-to-open Lifshitz transition induced by in-plane strain, from Ref. [29]. Note that, although it was calculated to occur at $\varepsilon_{xx} = -0.0075$, it was observed experimentally to occur at $\varepsilon_{xx} \approx -0.0044$ [28]. (b) Unstressed Sr_2RuO_4 . (c) The electron-to-hole Lifshitz transition predicted to occur under c -axis compression. (d) Calculation of the Fermi-level DOS against energy for a series of strains ε_{zz} . (e) Calculated Fermi-level DOS against ε_{zz} .

–5.5 GPa. Because meV-level energy shifts can substantially alter the distance to the Lifshitz transition, there is considerable uncertainty in these values [28]. The transition occurs approximately at the X and Y points of the Brillouin zone of the RuO_2 sheet, indicated in panel (c). We note also that while k_z warping increases on all the Fermi sheets, as expected for c -axis compression, the β sheet has the strongest k_z warping both at $\varepsilon_{zz} = 0$ and at the Lifshitz transition.

Experimental results

Four samples were measured. For good stress homogeneity, samples should be elongated along the stress axis, which is a challenge for the c axis because the cleave plane of Sr_2RuO_4 is the ab plane. A plasma focused ion beam, in which material is milled using a beam of Xe ions, was therefore used to shape the samples. Sample 1 was prepared with a uniform cross section, and a large enough stress, $\sigma_{zz} = -0.84$ GPa, was achieved to

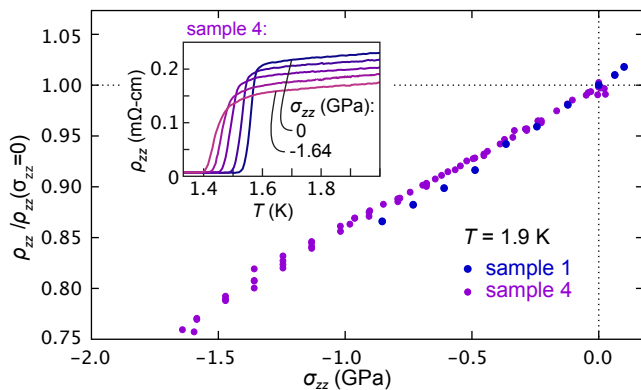


FIG. 2. Main panel: c -axis resistivity ρ_{zz} versus stress σ_{zz} at 1.9 K, normalized by its $\sigma_{zz} = 0$ value. Note that the stress scale of sample 1 is adjusted so that $dT_c/d\sigma_{zz}$ as measured through the Meissner effect matches that from sample 4 over the range $-0.92 < \sigma_{zz} < -0.2$ GPa. At $\sigma_{zz} = 0$, $\rho_{zz}(1.9 \text{ K})$ of samples 1 and 4 is 0.278 and 0.228 m Ω -cm, respectively. Inset: ρ_{zz} versus temperature for sample 4 at 0, -0.37 , -0.85 , -1.25 , and -1.64 GPa.

observe a clear change in T_c . To go further, the other samples were all sculpted into dumbbell shapes, with the wide ends providing large surfaces for coupling force into the sample. FIB microstructuring has been shown to be a powerful tool for studying stress-strain curves in micropillars of CaFe_2As_2 [37]. Here our goals were slightly different because we wanted to retain sufficient sample volume to enable high-precision magnetic susceptibility measurements. For measurement of T_c in the neck portion, two concentric coils of a few turns each were wound around the neck. Samples 1 and 4 also had electrical contacts, for measurement of the c -axis resistivity ρ_{zz} . Photographs of the samples are shown in the Methods section.

Sample 4 was measured in apparatus that incorporated a sensor of the force applied to the sample [38], from which the stress in the sample could be accurately determined. Samples 1–3 were mounted into apparatus that had a sensor only of the displacement applied to the sample, which is an imperfect measure of the sample strain because the sensor also picks up deformation in the epoxy. Therefore, a displacement-to-stress conversion was applied to samples 1–3 to bring the rate of change of T_c over the stress range $0.92 < \sigma_{zz} < -0.20$ GPa into agreement with that of sample 4. In other words, we impose on our data an assumption that the initial rate of decrease in T_c is the same in all the samples, which is reasonable because their zero-stress T_c 's are very similar: all are between 1.45 and 1.50 K.

We begin by showing resistivity data, in Fig. 2. The plotted resistivities are corrected for the expected stress-induced change in sample geometry (reduced length and increased width) under an assumption that stress and strain remain proportional, and using the low-

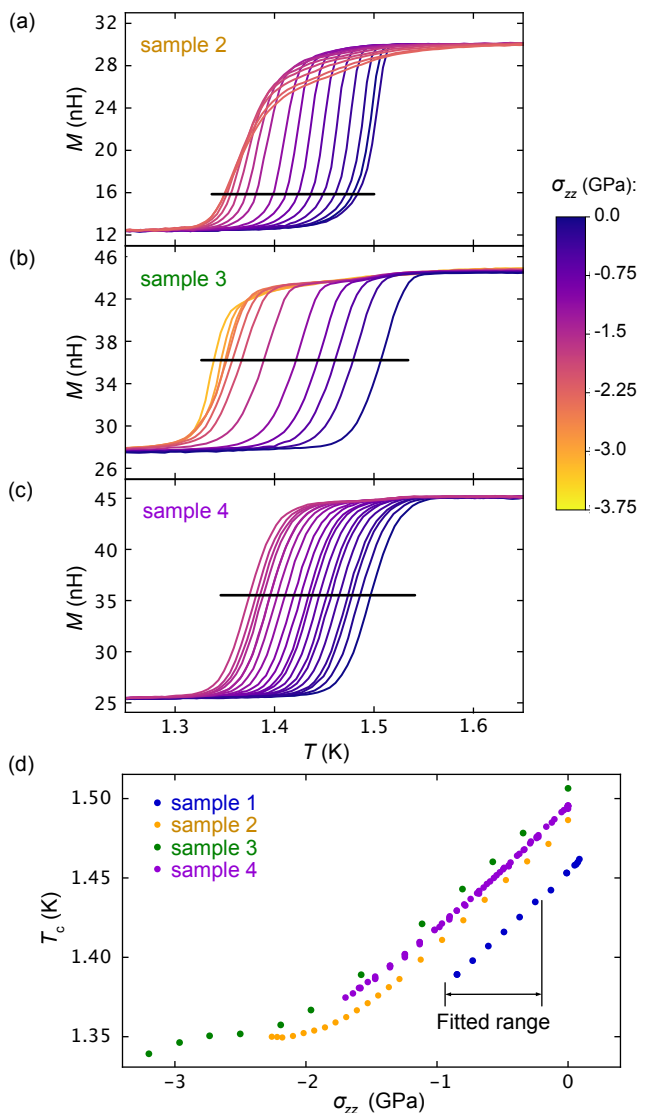


FIG. 3. (a–c) Raw data: mutual inductance M of the sense coils versus temperature for samples 2–4, at various applied stresses σ_{zz} . The lines indicate the selected thresholds for determination of T_c . For sample 2, under large $|\sigma_{zz}|$ a tail appears on the transitions, which we attribute to in-plane stress, and a low threshold is chosen to avoid this tail. (d) T_c versus stress for all the samples. The stress scales for samples 1–3 are scaled to bring $dT_c/d\sigma_{zz}$ into agreement with that of sample 4 over the stress range labeled “fitted range,” -0.92 to -0.20 GPa.

temperature elastic moduli reported in Ref. [35]. At zero stress the resistivity of sample 4 shows a sharp transition into the superconducting state at 1.55 K. This sharpness, and the fact that it only slightly exceeds the transition temperature seen in susceptibility, indicate high sample quality. With compression, T_c decreases. The normal-state resistivity also decreases, following the general expectations that c -axis compression should increase k_z dispersion.

We find elasto-resistivities $(1/\rho_{zz})d\rho_{zz}/d\varepsilon_{zz}$, obtained

with a linear fit over the range $-0.5 < \sigma_{zz} < 0$ GPa, of 37 and 32 for samples 1 and 4, respectively. Sample 4 was compressed to -1.7 GPa, and its resistivity does not show any major deviation from linearity over this range. There is some scatter in the data at large compression, which may be a consequence of cracking in the electrical contacts—we show below that the sample deformation was almost certainly elastic.

We now show the effects of interlayer compression on the superconductivity. In Fig. 3 we show the dependence of T_c measured through susceptibility on c -axis stress, for all four samples. Panels (a–c) show the actual transitions—the mutual inductance M of the sense coils versus temperature—for samples 2–4. To check that sample deformation remained elastic, we repeatedly cycled the stress to confirm that the form of the $M(T)$ curves remained unchanged; see the Appendix for examples. For samples 3 and 4, the transition remained narrow as stress was applied, indicating high stress homogeneity. For sample 2, there was a tail on the high-temperature side of the transition, that was stronger at higher compressions. We attribute it to in-plane strain, possibly originating in the fact that sample 2 was not as well aligned as samples 3 and 4. A similar, though weaker, tail is also visible for sample 3.

Panel (d) shows T_c versus stress for all the samples. T_c is taken as the temperature where M crosses a threshold. For samples 1, 3, and 4, we select a threshold at $\approx 50\%$ of the height of the transition, and for sample 2, 20%, in order to minimize the influence from the high-temperature tail. T_c is seen to decrease almost linearly out to $\sigma_{zz} \approx -1.8$ GPa. For sample 4 (to which, as described above, the other samples are referenced), $dT_c/d\sigma_{zz}$ in the limit $\sigma_{zz} \rightarrow 0$ is 76 ± 5 mK/GPa. The error is 6%: we estimate a 5% error on the calibration of the force sensor of the cell, and a 3% error on the cross-sectional area of the sample ($155 \times 106 \mu\text{m}^2$).

At $\sigma_{zz} \lesssim -1.8$ GPa, the stress dependence of T_c flattens markedly. In sample 3, T_c is seen to resume its decrease for $\sigma_{zz} < -3$ GPa. We show in the Methods section that both the flattening and this further decrease reproduce when the stress is cycled, which, in combination with the narrowness of the transitions, shows that this behavior is intrinsic, and not an artefact of any drift or non-elastic deformation in the system.

Fig. 4 shows measurements of the c -axis upper critical field. $M(H)$ for samples 2 and 3 at constant temperature $T \approx 0.3$ K is shown in panels (a) and (b). In Fig. 4(c), we plot H_{c2} versus stress, taking H_{c2} as the fields at which M crosses the thresholds indicated in panels (a–b). H_{c2} is seen to increase as stress is applied, as generally expected when the density of states increases. The increase is faster for sample 2 than sample 3, which may be an artefact of the tail on the transition for sample 2.

For an isotropic system, $H_{c2} \propto (T_c/v_F)^2$, where v_F is the Fermi velocity, and so in panel (d) we plot H_{c2}/T_c^2

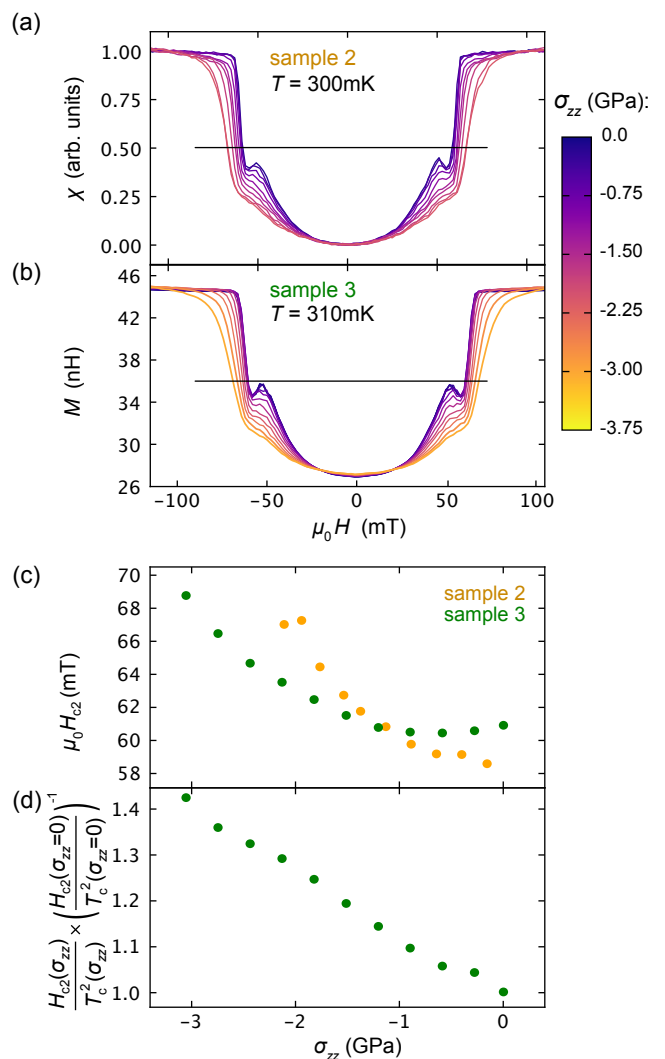


FIG. 4. (a–b) Susceptibility versus applied field $\parallel c$ for samples 2 and 3, at fixed temperatures of 300 mK and 310 mK. For sample 3, the raw data are plotted. For sample 2, the signal magnitude shifted from run to run, so data are normalized by the readings at 0 and 100 mT. This shift was probably due to motion of the coils against the sample; when they were fixed more securely to collect the data in Fig. 3(a), the problem disappeared. The horizontal lines indicate the thresholds for determination of H_{c2} . (c) $H_{c2}(T \approx 0.3$ K) versus stress for samples 2 and 3. (d) H_{c2}/T_c^2 , normalized by its zero-stress value, versus stress for sample 3.

normalized by its zero-stress value for sample 3. It increases by $\approx 40\%$ by $\sigma_{zz} = -3.0$ GPa, which, if the gap structure does not change drastically, suggests an increase in the Fermi-level DOS of $\approx 20\%$.

Another feature visible in the $M(H)$ traces of Fig. 4(a–b) is a peak effect—a local maximum in the susceptibility just below H_{c2} . It occurs when there is a range of temperature below T_c where vortex motion is uncorrelated, allowing individual vortices to find deeper pinning sites [39]. The peak is suppressed by c -axis compression, and it is suppressed downward rather than by be-

ing smeared horizontally along the H axis, which means that it is not an artefact of a spread of H_{c2} due to strain inhomogeneity. It could indicate stronger pinning, due to the reduction in the coherence length.

Weak-coupling calculations

To further investigate the opposing trends of T_c and H_{c2} , we supplement these results with weak-coupling calculations for repulsive Hubbard models, as developed in Refs. [40–49]. To capture possible changes in the 3D gap structure, we employ three-dimensional Fermi surfaces [50]. These are calculated using a tight-binding model for the three bands that cross the Fermi level, that takes the form

$$H_0 = \sum_{\mathbf{k}, s} \psi_s^\dagger(\mathbf{k}) \mathcal{H}_s(\mathbf{k}) \psi_s(\mathbf{k}). \quad (1)$$

$\psi_s(\mathbf{k}) = [c_{xz,s}(\mathbf{k}), c_{yz,s}(\mathbf{k}), c_{xy,\bar{s}}(\mathbf{k})]^T$, and $\mathcal{H}_s(\mathbf{k})$ incorporates spin-orbit coupling, inter-orbital and intra-orbital terms as extracted from the DFT calculations. The complete set of tight-binding parameters retained here is given in the Methods section. In Fig. 5(a), we show the tight-binding Fermi surfaces at $\varepsilon_{zz} = 0$ and -0.02 . In Fig. 5(b), we show the orbital weight on the γ sheet at $k_z = 0$. Because the γ sheet expands under c -axis compression, the orbital mixing around its avoided crossings with the β sheet is reduced, and it becomes more dominated by xy orbital weight.

To H_0 we add on-site Coulomb terms projected onto the t_{2g} orbitals [51] (Methods Eq. 7) and study the solutions to the linearized gap equation in the weak-coupling limit $U/t \ll 1$, where U is the intraorbital Coulomb repulsion and t is the leading tight-binding term. We take the interorbital on-site Coulomb repulsion to be $U' = U - 2J$, where J is the Hund's coupling, and the pair-hopping Hund's interaction J' to be equal to the spin-exchange Hund's interaction J . Under these assumptions, the remaining free parameter is J/U . We take $J/U = 0.15$, which is close to the value $J/U = 0.17$ found in Refs. [52, 53]. The linearized gap equation reads

$$\sum_{\nu} \int_{S_{\nu}} \frac{d\mathbf{k}_{\nu}}{|S_{\nu}|} \bar{\Gamma}(\mathbf{k}_{\mu}, \mathbf{k}_{\nu}) \varphi(\mathbf{k}_{\nu}) = \lambda \varphi(\mathbf{k}_{\mu}), \quad (2)$$

where μ and ν are band indices, $|S_{\nu}|$ is the area of Fermi surface sheet ν , and $\bar{\Gamma}$ is the two-particle interaction vertex calculated consistently to order $\mathcal{O}(U^2/t^2)$. Solutions to Eq. (2) with $\lambda < 0$ signal the onset of superconductivity, at the critical temperature $T_c \sim W \exp(-1/|\lambda|)$, where W is the bandwidth.

In a pseudo-spin basis each eigenvector φ belongs to one of the ten irreducible representations of the crystal point group D_{4h} [47, 54]. We calculate the leading eigenvalues in four even-parity channels, B_{1g} , B_{2g} , A_{1g} , and

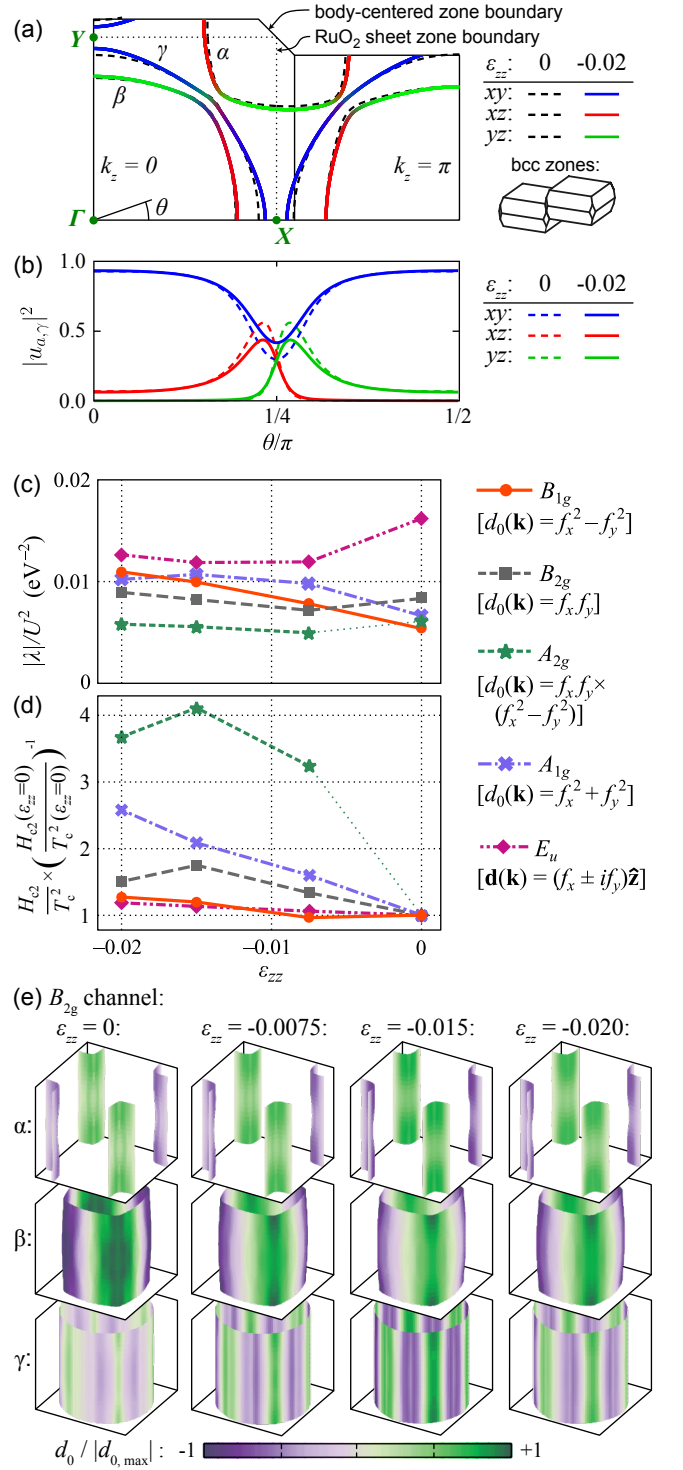


FIG. 5. (a) Cuts through the tight-binding Fermi surfaces employed in our weak-coupling calculations, at $\varepsilon_{zz} = 0$ and -0.02 . The surfaces at $\varepsilon_{zz} = -0.02$ are colored by orbital content. (b) Orbital weights on the γ sheet at $k_z = 0$ in this model. (c) Eigenvalues as a function of ε_{zz} for $J/U = 0.15$. In the legend, f_i is any function that transforms as $\sin k_i$; $d_0(\mathbf{k})$ is the gap function for the even-parity irreducible representations, and $\mathbf{d}(\mathbf{k})$ the d -vector for E_u . In the A_{2g} channel, there is a transition in the gap structure between $\varepsilon_{zz} = 0$ and -0.0075 . (d) $H_{c2}(T \rightarrow 0)/T_c^2$ versus ε_{zz} in each channel. (e) Gap structure in the B_{2g} channel.

A_{2g} — see the legend of Fig. 5(c–d). The E_g channel — $d_{xz} \pm id_{yz}$ — has been found to be strongly disfavored in weak-coupling calculations [50], and so is not considered here. We calculate only one odd-parity channel, E_u . The splitting among the odd-parity channels has been found to be small in comparison with that between odd- and even-parity states for reasonable values of J/U and spin-orbit coupling [55].

The leading eigenvalues in each channel as a function of ε_{zz} are shown in Fig. 5(c). Although, as in Ref. [50], odd-parity order is found to be favored, calculations in the random phase approximation at similar J/U tend to favor even-parity order [15, 55]. A tendency towards odd-parity order appears to be a feature of calculations in the weak-coupling limit.

The weak-coupling results show a dichotomy in the strain dependence of T_c : T_c in the channels that have symmetry-imposed nodes at the X and Y points (E_u , A_{2g} , and B_{2g}) decreases with initial c -axis compression. These nodes coincide with the regions of highest local density of states, and this result is an indication that order parameters in these channels are less able to take advantage of the increase in density of states induced by c -axis compression. We note, however, that under stronger compression T_c increases modestly in all the channels.

We also calculate H_{c2}/T_c^2 , following the procedure described in Ref. [29], and obtain the results shown in Fig. 5(d). We find that changes in H_{c2}/T_c^2 correlate closely with shifts in the gap weight onto the γ sheet, which has the lowest Fermi velocity. This is illustrated by the calculated gap structure in the B_{2g} channel, shown in Fig. 5(e); the gap structures in the other channels are shown in Methods Fig. 9. As stress is initially applied, gap weight shifts from the β to the γ sheet, to take advantage of the increasing DOS on the γ sheet. However, in this channel the gap changes sign across the zone boundary of the RuO_2 sheet, and so at the strongest compression, where γ sheets in adjacent zones come close to each other, the gap is suppressed on the γ sheet. The calculated H_{c2}/T_c^2 follows this non-monotonic dependence: an initial increase as gap weight shifts to the γ sheet, then a decrease as it shifts back. Under strong compression ($\varepsilon_{zz} < -0.015$ in this model), there is a clear dichotomy between the even-parity channels with and without nodes along Γ - X and Γ - Y : H_{c2}/T_c^2 decreases for the former and increases for the latter.

Although a k_z dependence of the gap structure is seen in all channels, we do not find dramatic stress-induced changes in the k_z dependence in any channel. Separately, in Fig. 5(d) a very strong increase in H_{c2}/T_c^2 is found in the A_{2g} channel. This is due to a first-order change in the gap structure, indicated in the figure by a dotted line.

DISCUSSION

The unexpected decrease of T_c with c -axis uniaxial pressure as two Van Hove singularities are approached is the key experimental result that we report. It might provide a vital clue to understand the nature of the superconducting state in Sr_2RuO_4 , because it is so different to the response to in-plane, a -axis pressure. To assess the significance of the differing results between the two pressure directions, we first examine the scale of the density of states increase that is being achieved in our c -axis pressure experiment.

An applied pressure of $\sigma_{zz} = -3.2$ GPa corresponds to a strain $\varepsilon_{zz} \approx -0.014$, about 60 % of that calculated to be necessary to cause a Lifshitz transition, -0.025 . However, there is considerable uncertainty in the calculated values, and so we also look at measured physical quantities to determine how far along the way to the electron-to-hole Lifshitz transition we reached. As noted above, H_{c2}/T_c^2 , a naive estimate of the square of the density of states, increases by 40 % between $\sigma_{zz} = 0$ and -3.0 GPa. For a axis pressure, the same 40 % increase occurs at approximately 65 % of the Lifshitz transition strain. These estimates highlight the scale of the discrepancy of the behaviour of T_c between the two directions of pressure: when H_{c2}/T_c^2 has risen by 40 % under a axis pressure, T_c has increased by 0.8 K. Here, with c -axis pressure T_c drops by 0.15 K. We are not aware of any two-dimensional model that has reproduced this behaviour. For example, the weak-coupling renormalization group study of Ref. [56] and functional renormalization group study of Ref. [57] both predict a rapid increase in T_c with approach to the electron-to-hole Lifshitz transition.

The response of T_c under c -axis compression also allows us to resolve the stress dependence of T_c into components by comparing it to the effect of hydrostatic compression, which also suppresses T_c linearly. We obtain the coefficients α and β in the expression

$$T_c = T_{c,0} + \alpha \times \frac{\Delta V}{V} + \beta \times \left(\varepsilon_{zz} - \frac{\varepsilon_{xx} + \varepsilon_{yy}}{2} \right),$$

where $\Delta V/V = \varepsilon_{xx} + \varepsilon_{yy} + \varepsilon_{zz}$ is the fractional volume change of the unit cell, and $\varepsilon_{zz} - (\varepsilon_{xx} + \varepsilon_{yy})/2$ is a volume-preserving tetragonal distortion. Refs. [12, 58, 59] report $dT_c/d\sigma_{\text{hydro}} = 0.22 \pm 0.02$, 0.24 ± 0.02 , and 0.21 ± 0.03 K/GPa; we take $dT_c/d\sigma_{\text{hydro}} = 0.23 \pm 0.01$ K/GPa. Employing the low-temperature elastic moduli from Ref. [35] to convert stress to strain, we find $\alpha = 34.8 \pm 1.6$ K and $\beta = -2.2 \pm 1.2$ K [60]. The small value of β means that a volume-preserving reduction in the lattice parameter ratio c/a would have little effect on T_c : the increase in density of states by approaching the electron-to-hole Lifshitz transition is balanced, somehow, by weakening of the pairing interaction. The challenge for theory is to understand how that weakening might take place.

In the three-dimensional weak-coupling calculations presented here, it is the A_{2g} and B_{2g} channels, both of which have nodes along the Γ - X and Γ - Y lines, that best match observations. Due to differences between the actual and calculated electronic structures the $\epsilon_{zz} = 0$ point in the calculations should not be considered too literally as equivalent to $\epsilon_{zz} = 0$ in reality, and the key point is that it is only in the A_{2g} and B_{2g} channels that T_c is found to decrease and H_{c2}/T_c^2 to increase over some range of strain. However, the A_{2g} and B_{2g} order parameters do not appear to be consistent with the results of in-plane uniaxial stress experiments, in which the strong increase in H_{c2} as the electron-to-open Lifshitz transition is approached indicates that there are not nodes near the X and Y points. Although it is informative to see the extra possibilities that adding the third dimension to the calculations open up, it therefore seems that this specific approach does not solve the mystery presented by the observations.

We believe that another possibility is worthy of further theoretical attention: if the superconductivity is driven by interorbital interactions [22–25], then T_c might decrease because c -axis compression reduces orbital mixing. The superconducting energy scale is too weak to induce substantial band mixing, and so the proximity of the γ and the β sheets, and the resulting mixing of xy and xz/yz orbital weight over substantial sections of Fermi surface, is crucial to these models [23]. We have noted that c -axis compression reduces this mixing, by pushing the γ and β sheets apart. In contrast, under in-plane uniaxial compression these sheets are pushed closer together along one direction and further apart along the other [61]. It would be interesting to see this investigated qualitatively in interorbital models that explicitly address the effects of both a - and c -axis compression.

In summary, we have demonstrated methods to apply uniaxial stress of multiple GPa along the interlayer axis of layered materials in samples large enough to permit high-precision magnetic susceptibility measurements. Under such a compression, we find that T_c decreases even though the Fermi-level DOS increases, in striking contrast to the effect of in-plane uniaxial stress. This contrast cannot be explained by current theoretical models and highlights the importance of extending current theories of superconductivity of Sr_2RuO_4 to realistically incorporate the third dimension. At a more general level, our findings motivate the use of out-of-plane stress as a powerful tool for investigation of other low dimensional strongly correlated systems. In Sr_2RuO_4 , we now see that, even though it is extremely anisotropic, working in a purely 2D approximation may not be sufficient to gain a full understanding of its superconductivity.

Acknowledgements. We thank Aline Ramires and Carsten Timm for helpful discussions, Markus König for training on the focused ion beam, and Felix Flicker for help with development and running of the code. F.J.,

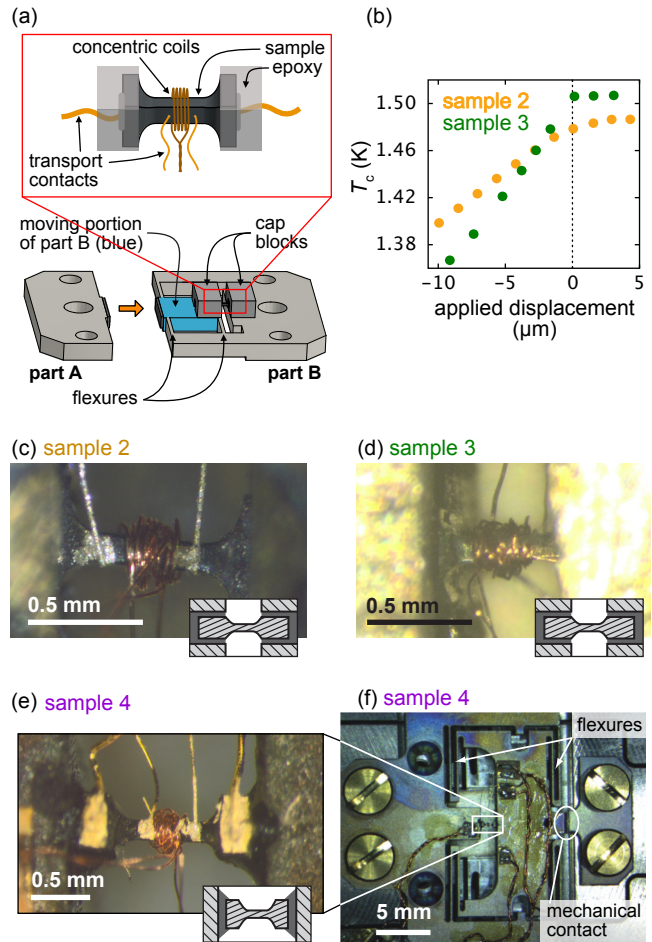


FIG. 6. (a) Schematic of the sample configuration for samples 2 and 3. These samples were sculpted into a dumbbell shape with a plasma focused ion beam. They were mounted with their ends embedded in epoxy. The cap blocks incorporate slots into which the sample fits, and the sample is compressed by bringing parts A and B into contact. (b) T_c versus applied displacement for samples 2 and 3. When parts A and B are brought into contact, force is applied to the sample, and T_c changes. (c–e) Photographs of samples 2, 3, and 4. The graphics at the lower right of each panel are schematic cross sections: the end tabs of samples 2 and 3 were epoxied into slots, while sample 4 was sandwiched between two surfaces. (f) A photograph of the sample carrier for sample 4.

A.P.M., and C.W.H. acknowledge the financial support of the Deutsche Forschungsgemeinschaft (DFG, German Research Foundation) - TRR 288 - 422213477 (project A10). H.S.R. and S.H.S. acknowledge the financial support of the Engineering and Physical Sciences Research Council (UK). H.S.R. acknowledges support from the Aker Scholarship. T.S. acknowledges the support of the Natural Sciences and Engineering Research Council of Canada (NSERC), in particular the Discovery Grant [RGPIN-2020-05842], the Accelerator Supplement [RGPAS-2020-00060], and the Discovery Launch Supplement [DGECR-2020-00222]. This research was enabled in part by support provided by Compute On-

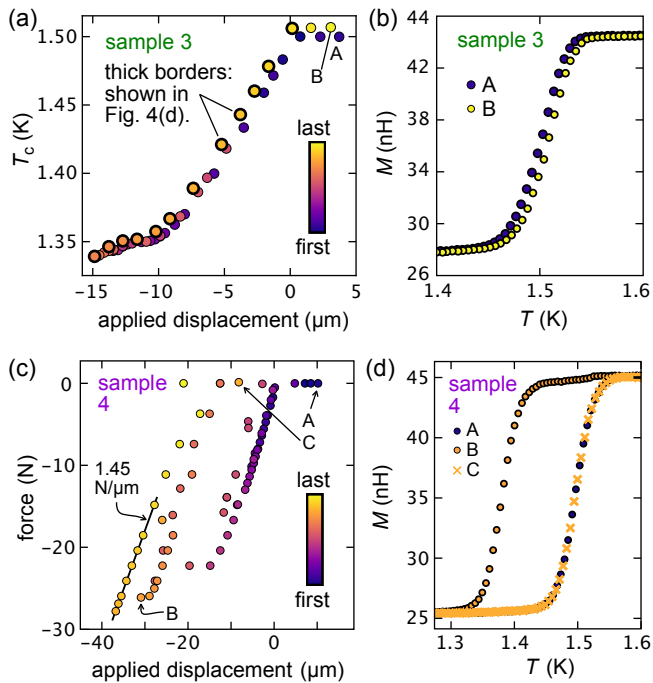


FIG. 7. (a) T_c of sample 3 versus applied displacement, with the data points colored by the order they were taken. The sequence of data points with the thick borders, during which $|\sigma_{zz}|$ was monotonically decreased, are those shown in Fig. 3(d). (b) Sense coil mutual inductance $M(T)$ at points A and B in the left-hand panel. (c) Force versus displacement of sample 4. (d) $M(T)$ at points A, B, and C in the left-hand panel.

tario (www.computeontario.ca) and Compute Canada (www.computecanada.ca). N.K. is supported by a KAKENHI Grants-in-Aids for Scientific Research (Grant Nos. 17H06136, 18K04715, and 21H01033), and Core-to-Core Program (No. JPJSCCA20170002) from the Japan Society for the Promotion of Science (JSPS) and by a JST-Mirai Program (Grant No. JPMJMI18A3). Raw data shown in this article are available at *website to be determined*.

METHODS

Experimental details

Sr_2RuO_4 samples were grown using a floating-zone method [62, 63]. The four samples here were taken from the same original rod, and from a portion that we verified to have high T_c and a low-density of Ru inclusions; our aim in taking multiple samples was to test re-productibility in sample preparation and mounting.

Uniaxial stress was applied using piezoelectric-driven apparatus [38, 64], and precision in sample mounting is important because Sr_2RuO_4 is much more sensitive to in-plane than c -axis uniaxial stress: T_c decreases by 0.13 K

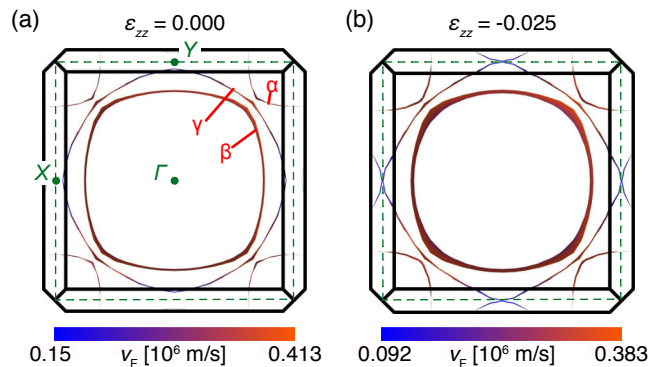


FIG. 8. Fermi surfaces of Sr_2RuO_4 projected along k_z under (a) zero stress and (b) $\epsilon_{zz} = -0.025$. The width of the lines indicates the warping of the Fermi surface along k_z . The dashed green line is the 2D zone boundary of the RuO_2 sheet.

under a c -axis stress of $\sigma_{zz} = -3.0 \text{ GPa}$, but increases by 0.13 K under an in-plane uniaxial stress of only 0.2 GPa [29]. Applying c -axis pressure could generate in-plane stress through bending and/or sample inhomogeneity. In a previous experiment [65], c -axis compression raised T_c and broadened the transition. However, the stress was applied at room temperature, where the elastic limit of Sr_2RuO_4 is low [38], so these effects may have been a consequence of in-plane strain due to defects introduced by the applied stress.

Samples 2–4 were mounted into two-part sample carriers; that for samples 2 and 3 is diagrammed in Fig. 6(a). The purpose was to protect samples from inadvertent application of tensile stress. Samples are mounted across a gap between a fixed and a moving portion of part B of the carrier, and can be compressed, but not tensioned, by bringing part A into contact with part B. In Fig. 6 (b), we show T_c of samples 2 and 3 versus applied displacement, and the point where parts A and B come into contact and T_c starts changing is clearly visible. For sample 2 the point of contact is rounded on the scale of a few microns, due to roughness and/or misalignment of the contact faces, and in all figures below we exclude data points that we estimate to be affected by this rounding.

The samples were mounted with Stycast 2850. This epoxy layer constitutes a conformal layer that ensures even application of stress [64]. Photographs of samples 2–4 are shown in Fig. 6(c–e). The carrier for sample 4, which has a different design to those used for samples 2 and 3, is shown in Fig. 6(f). Where electrical contacts were made, Du-Pont 6838 silver paste annealed at 450° for typically 30 minutes was used. This is longer than usual, in order to penetrate a thin insulating layer deposited during the ion beam milling.

As noted above, samples 1–3 were mounted in apparatus that had a sensor only of the displacement applied to the sample, while for sample 4 there was also a force sensor. Displacement sensors are less reliable as

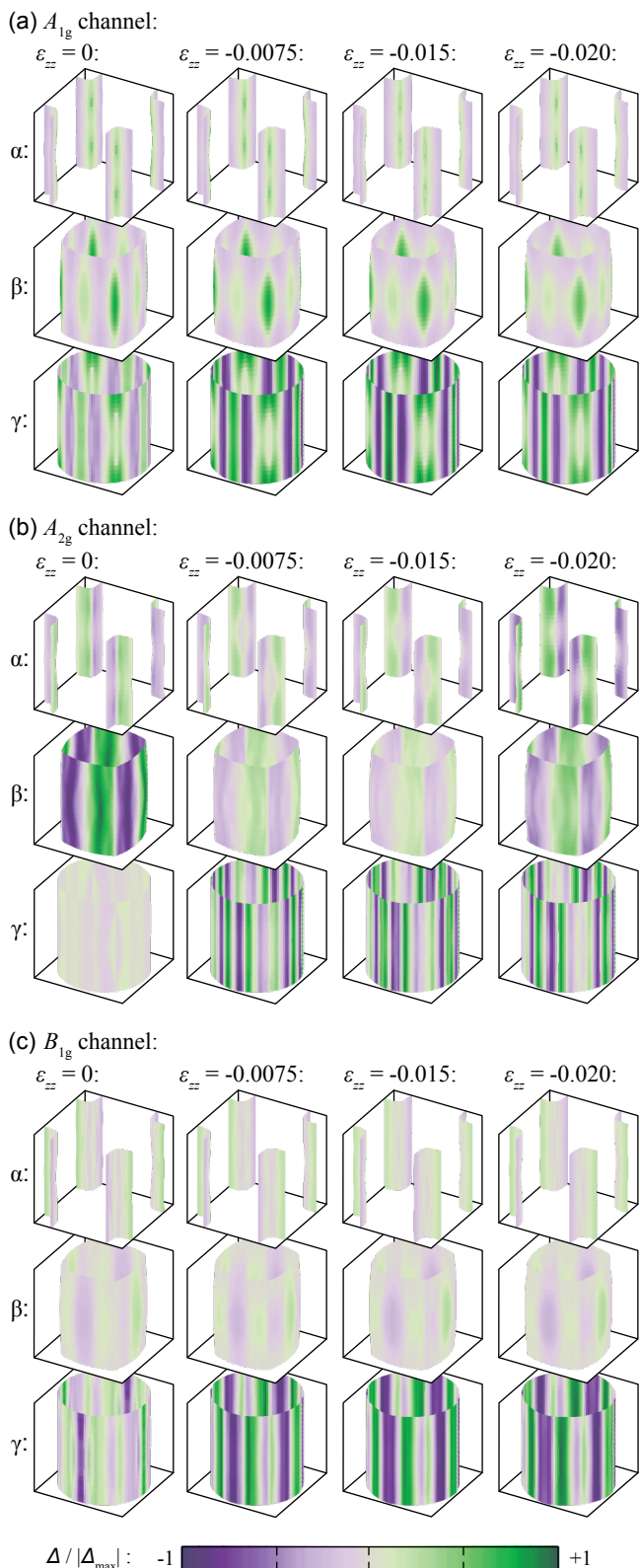


FIG. 9. Gap structures at $J/U = 0.15$ for, from top to bottom, the A_{1g} , A_{2g} , and B_{1g} channels, at the indicated strains. For each channel, the top, middle, and bottom rows show the gap on the α , β , and γ sheets, respectively.

sensors of the state of the sample, because they also pick up deformation of the epoxy that holds the sample. In Fig. 7(a) the complete set of measurements of T_c of sample 3, plotted against applied displacement, are shown. Data points are colored by the order in which they were collected. The data drifted leftward over time: stronger compression was needed to reach the same T_c . However, the qualitative form of the curve — initial decrease in T_c , then a flattening, and then further decrease — reproduced over multiple stress cycles, and in panel (b) it is shown that the form of the transition was the same before and after application of the strongest compression.

(We attribute the small apparent shift in T_c to an artefact of inadvertent mechanical contact between the stress cell and inner vacuum can of the cryostat.) We therefore conclude that the sample deformed elastically and that it was the epoxy holding the sample that was compressed non-elastically; plastic deformation has previously been observed to broaden the superconducting transition [66] of Sr_2RuO_4 . In Fig. 3, in the main text, we show only the data taken after the epoxy was maximally compressed. Force versus displacement data for sample 4 are shown in Fig. 7(c—d), and here it can be seen that there was very substantial non-elastic compression of the epoxy. As with sample 3, the shape of the superconducting transition in the Sr_2RuO_4 was the same before and after application of large stress. Over regions where the sample and epoxy deformed elastically, the combined spring constant was $1.45 \text{ N}/\mu\text{m}$. The spring constant of the flexures in the carrier, on the other hand, is calculated to be $\sim 0.03 \text{ N}/\mu\text{m}$, meaning that almost all of the applied force was transferred to the sample.

Electronic structure calculations

The calculated Fermi surfaces of unstressed Sr_2RuO_4 and under interlayer compression, including the warping along k_z and the Fermi velocities, are shown in Fig. 8. The β sheet is the most strongly warped both at zero stress and at $\epsilon_{zz} = -0.025$.

Estimate of c -axis strain by resistivity

In the DFT calculation, the increase in the DOS reaches 20 % at $\epsilon_{zz} \approx -0.017$, around 70 % of the way to the Lifshitz transition. The c -axis resistivity also allows an estimate of how close we are to the Lifshitz point. c -axis conductivity is proportional to the square of the amplitude of k_z warping. We observe ρ_{zz} to fall by 14–17% between $\sigma_{zz} = 0$ and -1.0 GPa , implying an increase in warping amplitude of 8–10%. The β sheet is the most strongly warped, and in the DFT calculations, its warping - its area projected on the $k_x - k_y$ plane - is 85% larger at the Lifshitz transition than at zero strain. Therefore,

if warping increases linearly with c -axis compression the Lifshitz transition is expected to occur between -8 and -11 GPa. In practice, the dependence on compression is likely to be super-linear, so we believe that taking into account the various pieces of evidence an estimate that we are approximately half way to the transition point is reasonable.

Calculated gap structure in other channels

In Fig. 9 the calculated gap structures in the A_{1g} , A_{2g} , and B_{1g} channels are shown. [The B_{2g} gap structures are shown in Fig. 5(e).] c -axis compression favors large gaps on the γ sheet in all channels. In the A_{2g} channel, this shift occurs as a first-order change in gap structure between $\epsilon_{zz} = 0$ and $\epsilon_{zz} = -0.0075$. At the largest compression reached, gap weight in the A_{2g} channel shifts back away from the γ sheet, as it does in the B_{2g} channel.

This does not occur in the A_{1g} and B_{1g} channels.

Details of the weak-coupling calculation

The tight-binding Hamiltonian from Eq. (1) takes the form

$$\mathcal{H}_s(\mathbf{k}) = \begin{pmatrix} \epsilon_{AA}(\mathbf{k}) & \epsilon_{AB}(\mathbf{k}) - is\eta_1 & +i\eta_2 \\ \epsilon_{BA}(\mathbf{k}) + is\eta_1 & \epsilon_{BB}(\mathbf{k}) & -s\eta_2 \\ -i\eta_2 & -s\eta_2 & \epsilon_{CC}(\mathbf{k}) \end{pmatrix}, \quad (3)$$

where we used the Ru orbital shorthand notation $A = xz$, $B = yz$, $C = xy$, and where $\bar{s} = -s$ (s being spin). In Eq. (3) the energies $\epsilon_{AB}(\mathbf{k})$ account for intra-orbital ($A = B$) and inter-orbital ($A \neq B$) hopping, and η_1 , η_2 parametrize the spin-orbit coupling. We define $\epsilon_{AA}(\mathbf{k}) = \epsilon_{1D}(k_x, k_y, k_z)$, $\epsilon_{BB}(\mathbf{k}) = \epsilon_{1D}(k_y, k_x, k_z)$, and $\epsilon_{CC}(\mathbf{k}) = \epsilon_{2D}(k_x, k_y, k_z)$, and we retain the following terms in the matrix elements:

$$\begin{aligned} \epsilon_{1D}(k_{\parallel}, k_{\perp}, k_z) &= -\mu_{1D} - 2t_1 \cos(k_{\parallel}) - 2t_2 \cos(k_{\perp}) - 4t_3 \cos(k_{\parallel}) \cos(k_{\perp}) \\ &\quad - 8t_4 \cos(k_{\parallel}/2) \cos(k_{\perp}/2) \cos(k_z/2) - 2t_5 \cos(2k_{\parallel}) - 4t_6 \cos(2k_{\parallel}) \cos(k_{\perp}) - 2t_7 \cos(3k_{\parallel}), \end{aligned} \quad (4)$$

$$\begin{aligned} \epsilon_{2D}(\mathbf{k}) &= -\mu_{2D} - 2\bar{t}_1 [\cos(k_x) + \cos(k_y)] - 2\bar{t}_2 [\cos(2k_x) + \cos(2k_y)] - 4\bar{t}_3 \cos(k_x) \cos(k_y) \\ &\quad - 4\bar{t}_4 [\cos(2k_x) \cos(k_y) + \cos(2k_y) \cos(k_x)] - 4\bar{t}_5 \cos(2k_x) \cos(2k_y) \\ &\quad - 4\bar{t}_6 [\cos(3k_x) \cos(k_y) + \cos(3k_y) \cos(k_x)] - 2\bar{t}_7 [\cos(3k_x) + \cos(3k_y)] \\ &\quad - 8\bar{t}_8 \cos(k_z/2) \cos(k_x/2) \cos(k_y/2), \end{aligned} \quad (5)$$

$$\epsilon_{AB}(\mathbf{k}) = -8\bar{t} \sin(k_x/2) \sin(k_y/2) \cos(k_z/2). \quad (6)$$

Here the first Brillouin zone is defined as $\text{BZ} = [-\pi, \pi]^2 \times [-2\pi, 2\pi]$. For the four values of c -axis compression $\epsilon_{zz} = 0, -0.0075, -0.015, -0.020$ we extract the entire set of

parameters from DFT calculations consistent with Fig. 1; see Table I.

For the interactions we use the (on-site) Hubbard-Kanamori Hamiltonian

$$H_I = \frac{U}{2} \sum_{i,a,s \neq s'} n_{ias} n_{ias'} + \frac{U'}{2} \sum_{i,a \neq b,s,s'} n_{ias} n_{ibs'} + \frac{J}{2} \sum_{i,a \neq b,s,s'} c_{ias}^\dagger c_{ibs'}^\dagger c_{ias'} c_{ibs} + \frac{J'}{2} \sum_{i,a \neq b,s \neq s'} c_{ias}^\dagger c_{ias'}^\dagger c_{ibs'} c_{ibs}, \quad (7)$$

where i is site, a is orbital, and $n_{ias} = c_{ias}^\dagger c_{ias}$ is the density operator. We further assume that $U' = U - 2J$ and $J' = J$ [51]. In the weak-coupling limit this leaves J/U as a single parameter fully characterizing the interactions.

In the linearized gap equation (2) the (dimensionless)

two-particle interaction vertex $\bar{\Gamma}$ is defined as [47]

$$\bar{\Gamma}(\mathbf{k}_\mu, \mathbf{k}_\nu) = \sqrt{\frac{\rho_\mu \bar{v}_\mu}{v_\mu(\mathbf{k}_\mu)}} \Gamma(\mathbf{k}_\mu, \mathbf{k}_\nu) \sqrt{\frac{\rho_\nu \bar{v}_\nu}{v_\nu(\mathbf{k}_\nu)}}, \quad (8)$$

where $\rho_\mu = |S_\mu|/[\bar{v}_\mu(2\pi)^3]$ is the density of states, and $1/\bar{v}_\mu = \int_{S_\mu} d\mathbf{k}/(|S_\mu|v_\mu(\mathbf{k}))$. Here, Γ is the irreducible two-particle interaction vertex which to leading order retains the diagrams shown in Fig. 10.

An eigenfunction φ of Eq. (2) corresponding to a neg-

TABLE I. Tight-binding parameters (in units of meV) used for Eqs. (3), (4), (5), and (6), yielding Fig. 5(a).

| $ \varepsilon_{zz} $ | μ_{1D} | t_1 | t_2 | t_3 | t_4 | t_5 | t_6 | t_7 | μ_{2D} | \bar{t}_1 | \bar{t}_2 | \bar{t}_3 | \bar{t}_4 | \bar{t}_5 | \bar{t}_6 | \bar{t}_7 | \bar{t}_8 | \bar{t} | η_1 | η_2 |
|----------------------|------------|-------|-------|-------|-------|-------|-------|-------|------------|-------------|-------------|-------------|-------------|-------------|-------------|-------------|-------------|-----------|----------|----------|
| 0.00 | 316 | 296 | 53 | -16 | 17 | -57 | -15 | -12 | 433 | 370 | -6 | 123 | 20 | 14 | 3 | 3 | -2 | 9 | -51 | -51 |
| 0.0075 | 294 | 284 | 54 | -16 | 18 | -56 | -15 | -10 | 437 | 369 | -5 | 122 | 20 | 14 | 3 | 3 | -3 | 10 | -51 | -51 |
| 0.015 | 273 | 271 | 55 | -17 | 19 | -55 | -15 | -9 | 441 | 368 | -5 | 121 | 20 | 13 | 3 | 3 | -3 | 10 | -51 | -51 |
| 0.020 | 259 | 264 | 56 | -18 | 20 | -55 | -15 | -8 | 443 | 367 | -4 | 120 | 20 | 13 | 3 | 3 | -3 | 11 | -52 | -51 |

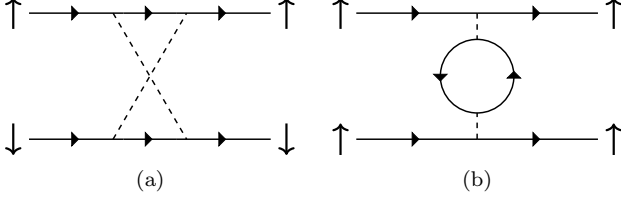


FIG. 10. Second-order diagrams taken into account in Γ in (a) the even-parity channel, and (b) the odd-parity channel. The vertical arrows denote pseudo-spin, and the dashed lines contain all the terms of Eq. (7). The approach is asymptotically exact in the weak-coupling limit, $U/t \rightarrow 0$.

ative eigenvalue λ yields the superconducting order parameter

$$\Delta(\mathbf{k}_\mu) \sim \sqrt{\frac{v_\mu(\mathbf{k}_\mu)}{\bar{v}_\mu \rho_\mu}} \varphi(\mathbf{k}_\mu). \quad (9)$$

In the chosen pseudo-spin basis each eigenvector φ belongs to one of the ten irreducible representations of the crystal point group D_{4h} [47, 54].

[1] Y. Maeno, H. Hashimoto, K. Yoshida, S. Nishizaki, T. Fujita, J. G. Bednorz, and F. Lichtenberg, *Nature* **372**, 532 (1994).
[2] A. P. Mackenzie and Y. Maeno, *Rev. Mod. Phys.* **75**, 657 (2003).
[3] Y. Maeno, S. Kittaka, T. Nomura, S. Yonezawa, and K. Ishida, *J. Phys. Soc. Japan* **81**, 011009 (2012).
[4] A. P. Mackenzie, T. Scaffidi, C. W. Hicks, and Y. Maeno, *npj Quant. Mat.* **2**, 40 (2017).
[5] A. Pustogow, Y. K. Luo, A. Chronister, Y.-S. Su, D. A. Sokolov, F. Jerzembeck, A. P. Mackenzie, C. W. Hicks, N. Kikugawa, S. Raghu, E. D. Bauer, and S. E. Brown, *Nature* **574**, 72 (2019).
[6] K. Ishida, M. Manago, K. Kinjo, and Y. Maeno, *J. Phys. Soc. Japan* **89**, 034712 (2020).
[7] A. Chronister, A. Pustogow, N. Kikugawa, D. A. Sokolov, F. Jerzembeck, C. W. Hicks, A. P. Mackenzie, E. D. Bauer, and S. E. Brown, *Proc. Nat. Acad. Sci. USA* **118**, e2025313118 (2021).
[8] A. N. Petsch, M. Zhu, M. Enderle, Z. Q. Mao, Y. Maeno, I. I. Mazin, and S. M. Hayden, *Phys. Rev. Lett.* **125**, 217004 (2020).
[9] G. M. Luke, Y. Fudamoto, K. M. Kojima, M. I. Larkin, J. Merrin, B. Nachumi, Y. J. Uemura, Y. Maeno, Z. Q.

Mao, Y. Mori, H. Nakamura, and M. Sgrist, *Nature* **394**, 558 (1998).
[10] V. Grinenko, S. Ghosh, R. Sarkar, J.-C. Orain, A. Nikitin, M. Elender, D. Das, Z. Guguchia, F. Brückner, M. E. Barber, J. Park, N. Kikugawa, D. A. Sokolov, J. Bobowski, T. Miyoshi, Y. Maeno, A. P. Mackenzie, H. Luetkens, C. W. Hicks, and H.-H. Klauss, *Nat. Physics* **17**, 748 (2021).
[11] J. Xia, Y. Maeno, P. T. Beyersdorf, M. M. Fejer, and A. Kapitulnik, *Phys. Rev. Lett.* **97**, 167002 (2006).
[12] V. Grinenko, D. Das, B. Zinkl, N. Kikugawa, Y. Maeno, C. W. Hicks, H.-H. Klauss, M. Sgrist, and R. Khasanov, *Nat. Comm.* **12**, 3920 (2021).
[13] C. Bergemann, A. P. Mackenzie, S. R. Julian, D. Forsythe, and E. Ohmichi, *Advances in Physics* **52**, 639 (2003).
[14] E. Ohmichi, Y. Maeno, S. Nagai, Z. Mao, M. Tanatar, and T. Ishiguro, *Phys. Rev. B* **61**, 7101 (2000).
[15] A. T. Rømer, D. D. Scherer, I. M. Eremin, P. J. Hirschfeld, and B. M. Andersen, *Phys. Rev. Lett.* **123**, 247001 (2019).
[16] A. T. Rømer, P. J. Hirschfeld, and B. M. Andersen, *Phys. Rev. B* **104**, 064507 (2021).
[17] S. A. Kivelson, A. C. Yuan, B. Ramshaw, and R. Thomale, *npj Quantum Materials* **5**, 43 (2020).
[18] G. Wagner, H. S. Røising, F. Flicker, and S. H. Simon, *Phys. Rev. B* **104**, 134506 (2021).
[19] T. Scaffidi, arxiv:2007.13769 (2020).
[20] R. Willa, M. Hecker, R. M. Fernandes, and J. Schmalian, *Phys. Rev. B* **104**, 024511 (2021).
[21] Y.-S. Li, N. Kikugawa, D. A. Sokolov, F. Jerzembeck, A. S. Gibbs, Y. Maeno, C. W. Hicks, J. Schmalian, M. Nicklas, and A. P. Mackenzie, *Proc. Nat. Acad. Sci. USA* **118**, e2020492118 (2021).
[22] H.-G. Suh, H. Menke, P. M. R. Brydon, C. Timm, A. Ramires, and D. F. Agterberg, *Phys. Rev. Res.* **2**, 032023(R) (2020).
[23] J. Clepkens, A. W. Lindquist, and H.-Y. Kee, *Phys. Rev. Res.* **3**, 013001 (2021).
[24] O. Gingras, R. Nourafkan, A.-M. S. Tremblay, and M. Côté, *Phys. Rev. Lett.* **123**, 217005 (2019).
[25] A. Ramires and M. Sgrist, *Phys. Rev. B* **100**, 104501 (2019).
[26] R. Sharma, S. D. Edkins, Z. Wang, A. Kostin, C. Sowe, Y. Maeno, A. P. Mackenzie, J. C. S. Davis, and V. Madhavan, *Proc. Nat. Acad. Sci. USA* **117**, 5222 (2020).
[27] E. Hassinger, P. Bourgeois-Hope, H. Taniguchi, S. R. de Cotret, G. Grissonnanche, M. S. Anwar, Y. Maeno, N. Doiron-Leyraud, and L. Taillefer, *Phys. Rev. X* **7**, 011032 (2017).
[28] M. E. Barber, F. Lechermann, S. V. Streltsov, S. L. Skornyakov, S. Ghosh, B. J. Ramshaw, N. Kikugawa, D. A. Sokolov, A. P. Mackenzie, C. W. Hicks, and I. I. Mazin,

- Phys. Rev. B **100**, 245139 (2019).
- [29] A. Steppke, L. Zhao, M. E. Barber, T. Scaffidi, F. Jerzembeck, H. Rosner, A. S. Gibbs, Y. Maeno, S. H. Simon, A. P. Mackenzie, and C. W. Hicks, *Science* **355**, eaaf9398 (2017).
- [30] B. Burganov, C. Adamo, A. Mulder, M. Uchida, P. D. C. King, J. W. Harter, D. E. Shai, A. S. Gibbs, A. P. Mackenzie, R. Uecker, M. Bruetzam, M. Beasley, C. Fennie, D. Schlom, and K. Shen, *Phys. Rev. Lett.* **116**, 197003 (2016).
- [31] N. Kikugawa, A. P. Mackenzie, C. Bergemann, R. A. Borzi, S. A. Grigera, and Y. Maeno, *Phys. Rev. B* **70**, 060508(R) (2004).
- [32] N. Kikugawa, C. Bergemann, A. P. Mackenzie, and Y. Maeno, *Physical Review B* **70**, 134520 (2004).
- [33] K. M. Shen, N. Kikugawa, C. Bergemann, L. Balicas, F. Baumberger, W. Meevasana, N. J. C. Ingle, Y. Maeno, Z.-X. Shen, and A. P. Mackenzie, *Phys. Rev. Lett.* **99**, 187001 (2007).
- [34] O. Chmaissem, J. D. Jorgensen, H. Shaked, S. Ikeda, and Y. Maeno, *Phys. Rev. B* **57**, 5067 (1998).
- [35] S. Ghosh, A. Shekhter, F. Jerzembeck, N. Kikugawa, D. A. Sokolov, M. Brando, A. P. Mackenzie, C. W. Hicks, and B. J. Ramshaw, *Nat. Physics* **17**, 199 (2021).
- [36] H. Eschrig, M. Richter, and I. Opahle, in *Relativistic Electronic Structure Theory, Part II. Applications*, Theoretical and Computational Chemistry, Vol. 13, edited by P. Schwerdtfeger (Elsevier, 2004) pp. 723–776.
- [37] J. T. Sypek, H. Yu, K. J. Dusoe, G. Drachuck, H. Patel, A. M. Giroux, A. I. Goldman, A. Kreyssig, P. C. Canfield, S. L. Bud'ko, C. R. Weinberger, and S.-W. Lee, *Nat. Comm.* **8**, 1083 (2017).
- [38] M. E. Barber, A. Steppke, A. P. Mackenzie, and C. W. Hicks, *Rev. Sci. Inst.* **90**, 023904 (2019).
- [39] K. Yamazaki, M. Tokunaga, T. Tamegai, Z. Q. Mao, Y. Maeno, and S. Okayasu, *Physica C* **378-381**, 537 (2002).
- [40] W. Kohn and J. M. Luttinger, *Phys. Rev. Lett.* **15**, 524 (1965).
- [41] M. A. Baranov and M. Y. Kagan, *Z. Phys. B* **86**, 237 (1992).
- [42] M. Y. Kagan and A. Chubukov, *JETP Lett.* **50**, 517 (1989).
- [43] A. V. Chubukov and J. P. Lu, *Phys. Rev. B* **46**, 11163 (1992).
- [44] M. A. Baranov, A. V. Chubukov, and M. Yu. Kagan, *Int. J. Mod. Phys. A* **06**, 2471 (1992).
- [45] H. Fukazawa and K. Yamada, *J. Phys. Soc. Jpn.* **71**, 1541 (2002).
- [46] R. Hlubina, *Phys. Rev. B* **59**, 9600 (1999).
- [47] S. Raghu, S. A. Kivelson, and D. J. Scalapino, *Phys. Rev. B* **81**, 224505 (2010).
- [48] S. Raghu, A. Kapitulnik, and S. A. Kivelson, *Phys. Rev. Lett.* **105**, 136401 (2010).
- [49] T. Scaffidi, J. C. Romers, and S. H. Simon, *Phys. Rev. B* **89**, 220510 (2014).
- [50] H. S. Røising, T. Scaffidi, F. Flicker, G. F. Lange, and S. H. Simon, *Phys. Rev. Research* **1**, 033108 (2019).
- [51] E. Dagotto, T. Hotta, and A. Moreo, *Phys. Rep.* **344**, 1 (2001).
- [52] J. Mravlje, M. Aichhorn, T. Miyake, K. Haule, G. Kotliar, and A. Georges, *Phys. Rev. Lett.* **106**, 096401 (2011).
- [53] A. Tamai, M. Zingl, E. Rozbicki, E. Cappelli, S. Riccò, A. de la Torre, S. McKeown Walker, F. Y. Bruno, P. D. C. King, W. Meevasana, M. Shi, M. Radović, N. C. Plumb, A. S. Gibbs, A. P. Mackenzie, C. Berthod, H. U. R. Strand, M. Kim, A. Georges, and F. Baumberger, *Phys. Rev. X* **9**, 021408 (2019).
- [54] M. Sigrist and K. Ueda, *Rev. Mod. Phys.* **63**, 239 (1991).
- [55] Z. Wang, X. Wang, and C. Kallin, *Phys. Rev. B* **101**, 064507 (2020).
- [56] Y.-T. Hsu, W. Cho, A. F. Rebola, B. Burganov, C. Adamo, K. M. Shen, D. G. Schlom, C. J. Fennie, and E.-A. Kim, *Phys. Rev. B* **94**, 045118 (2016).
- [57] Y.-C. Liu, W.-S. Wang, F.-C. Zhang, and Q.-H. Wang, *Phys. Rev. B* **97**, 224522 (2018).
- [58] D. Forsythe, S. R. Julian, C. Bergemann, E. Pugh, M. J. Steiner, P. L. Alireza, G. J. McMullan, F. Nakamura, R. K. W. Haselwimmer, I. R. Walker, S. S. Saxena, G. G. Lonzarich, A. P. Mackenzie, Z. Q. Mao, and Y. Maeno, *Phys. Rev. Lett.* **89**, 166402 (2002).
- [59] O. Svitelskiy, S. Headley, S. W. Tozer, E. C. Palm, T. P. Murphy, D. Shulyatev, and A. V. Suslov, *Phys. Rev. B* **77**, 052502 (2008).
- [60] Under hydrostatic stress, $\sigma_{zz} = (396 \text{ GPa}) \times \varepsilon_{zz}$ and $\varepsilon_{xx} = 0.814\varepsilon_{zz}$.
- [61] V. Sunko, E. A. Morales, I. Marković, M. E. Barber, D. Milosavljević, F. Mazzola, D. A. Sokolov, N. Kikugawa, C. Cacho, P. Dudin, H. Rosner, C. W. Hicks, P. D. C. King, and A. P. Mackenzie, *npj Quantum Materials* **4**, 46 (2019).
- [62] Z. Q. Mao, Y. Maeno, and H. Fukazawa, *Mater. Res. Bull.* **35**, 1813 (2000).
- [63] J. S. Bobowski, N. Kikugawa, T. Miyoshi, H. Suwa, H.-S. Xu, S. Yonezawa, D. A. Sokolov, A. P. Mackenzie, and Y. Maeno, *Condens. Matter.* **4**, 6 (2019).
- [64] C. W. Hicks, M. E. Barber, S. D. Eddins, D. O. Brodsky, and A. P. Mackenzie, *Rev. Sci. Inst.* **85**, 065003 (2014).
- [65] S. Kittaka, H. Taniguchi, S. Yonezawa, H. Yaguchi, and Y. Maeno, *Physical Review B* **81**, 180510 (2010).
- [66] H. Taniguchi, K. Nishimura, S. K. Goh, S. Yonezawa, and Y. Maeno, *J. Phys. Soc. Japan* **84**, 014707 (2015).